Energy Flux Observations in an Internal Tide Beam in the Eastern North Atlantic

Janna Köhler[1] , **Maren Walter**[1] , **Christian Mertens**[2] , **Jan Stiehler**[1] , **Zhuhua Li**[3], **Zhongxiang Zhao**[4] , **Jin-Song von Storch**[3] , **and Monika Rhein**[1]

[1]MARUM—Center for Marine Environmental Sciences/Institute of Environmental Physics, University of Bremen, Bremen, Germany, [2]Institute of Environmental Physics, University of Bremen, Bremen, Germany, [3]Max Planck Institute for Meteorology, Hamburg, Germany, [4]Applied Physics Laboratory, University of Washington, Seattle, WA, USA

Abstract Low-mode internal waves propagate over large distances and provide energy for turbulent mixing when they break far from their generation sites. A realistic representation of the oceanic energy cycle in ocean and climate models requires a consistent implementation of their generation, propagation, and dissipation. Here we combine the long-term mean energy flux from satellite altimetry with results from a $1/10°$ global ocean general circulation model that resolves the low modes of internal waves and in situ observations of stratification and horizontal currents to study energy flux and dissipation along a 1000 km internal tide beam in the eastern North Atlantic. Internal wave fluxes were estimated from twelve 36- to 48-hr stations in along- and across-beam direction to resolve both the inertial period and tidal cycle. The observed internal tide energy fluxes range from 5.9 kW m^{-1} near the generation sites to 0.5 kW m^{-1} at distant stations. Estimates of energy dissipation come from both finestructure and upper ocean microstructure profiles and range, vertically integrated, from 0.5 to 3.3 mW m^{-2} along the beam. Overall, the in situ observations confirm the internal tide pattern derived from satellite altimetry, but the in situ energy fluxes are more variable and decrease less monotonically along the beam. Internal tides in the model propagate over shorter distances compared to results from altimetry and in situ measurements, but more spatial details close the main generation sites are resolved.

Plain Language Summary Internal tides are generated when a tidal wave strikes underwater hills, seamounts, or slopes. These internal waves carry energy through the oceans' basins and finally mix the water when they break. It is important for ocean and climate models to realistically simulate the behavior of these waves, because the patterns of mixing in the ocean matter for the climate. In this study we use observations from ships and satellites and the results of a global ocean model to calculate the transport and loss of energy by internal tidal waves in a region where they are particularly strong, south of the Azores islands in the northeast Atlantic. The tidal waves lose a part of their energy and cause some mixing along their path, but most of the energy remains several hundreds of kilometers away from their generation site. Internal tides in the model propagate over shorter distances compared to the observations from satellite and ships, but it resolves more spatial details close the main generation sites.

1. Introduction

The main power input into the oceanic internal wave field occurs through barotropic tides, which flow over sloping topography and generate propagating internal tides, wind forcing, which generates waves near the Coriolis frequency f, and extraction of energy from the geostrophically balanced flow by interaction with the topography. A cascade of dynamical processes ultimately leads to turbulent mixing and viscous dissipation at small scales in the interior and the boundaries of the ocean.

Internal tides are generated in areas where the barotropic tide interacts with rough or steep topography, and the global pattern of internal tide generation is a product of topographic roughness, tidal strength, and stratification. On the global scale, the low-mode waves (wavelengths of a few kilometers to about 100 to 200 km, group velocities in the order of 1 m s^{-1}) carry a major part of the energy converted from the barotropic tide (e.g., Falahat et al., 2014), but in regions of rough small-scale topography such as mid-ocean ridges (Falahat et al., 2014; St. Laurent & Garrett, 2002; Vic et al., 2018, 2019) or eddy-slope interaction such as western boundaries (Clément et al., 2016; Köhler et al., 2013), more energy can be contained in higher

modes. The higher mode waves break near the generation region and dissipate locally (e.g., Klymak et al., 2008; Vic et al., 2019), while low-mode internal tides as well as the wind generated near-inertial waves can radiate far away from their sources (e.g., Alford, 2003a; Alford & Zhao, 2007a). First frameworks to estimate global maps of internal tide energy sinks start to emerge (de Lavergne et al., 2019), but it is still challenging to observe where and when these waves break and to properly include them in ocean general circulation models (OGCMs).

With increasing computer power, high-resolution concurrent simulations of circulations and tides have become an important alternative for studying low-mode internal tides in a realistic setting of the global oceans. These simulations have been carried out using the 1/12.5° HYCOM model (Arbic et al., 2010, 2012) and the 1/10° MPIOM model (Müller et al., 2012). The latter is known as the STORMTIDE simulation. The internal tides' signatures in sea surface height simulated by both models compare well with those found in the altimetry data (Arbic et al., 2010, 2012; Müller et al., 2012). The characteristics of the M_2 and K_1 internal tides in STORMTIDE are further studied in detail by Li et al. (2015, 2017).

To account for an energy source for the diapycnal mixing caused by breaking internal waves in OGCMs, the energetically consistent parameterization IDEMIX (Internal Wave Dissipation, Energy and Mixing) was developed and subsequently refined (Eden & Olbers, 2014; Olbers & Eden, 2013; Pollmann et al., 2017). Such a parameterization as IDEMIX requires the input of all energy sources for internal waves, such as tidal energy and wind. In the case of tides, a global distribution of the conversion rates from barotropic to baroclinic energy, as well as the propagation direction of the generated internal tides, is needed. The global distributions of conversion rates from barotropic to baroclinic tidal energies are commonly diagnosed using numerical as well as analytical models combined with bathymetry datasets and climatologies of stratification (e.g., Jayne & St Laurent, 2001; Müller, 2013; Nycander, 2005; Simmons et al., 2004). The distribution of horizontal fluxes is somewhat known (Alford, 2003a; Alford & Zhao, 2007a; Zhao et al., 2016) but on a global scale limited by the small number of observations. Local budgets have been published for the South China Sea (Alford et al., 2015) and a part of the Mid-Atlantic Ridge (Vic et al., 2018).

In the framework of an integrated effort to improve the energy cycles in climate models, the TRR181 "Energy Transfers in Atmosphere and Ocean" (www.trr-energytransfers.de), a process study was conducted along paths where satellite altimetry shows a beam of elevated internal tide energy fluxes. In the eastern North Atlantic, the Azores islands and the Great Meteor Seamount Chain directly south of them stand out as a generation site of internal tides similar to Hawaii in the North Pacific (Figure 1a). This site has the advantage of being located in the subtropical gyre away from strong currents, which minimizes refraction of low-mode waves by mesoscale features and leaves topographic scattering and nonlinear wave-wave interactions (e.g., parametric subharmonic instability [PSI]) as the main processes for energy dissipation. The energy input into the ocean in this area is dominated by the barotropic-to-baroclinic conversion of internal tides; the recent study of Whalen et al. (2018) suggests that there is a seasonality in near-inertial waves in the subtropical gyre, but in the global comparison, the wind energy input into the internal wave field is low in the eastern subtropical Atlantic (Alford, 2003b; Rimac et al., 2013).

The constructive interference of internal tides that are generated by multiple sources can form beams of internal tide energy flux (Rainville et al., 2010). Maps of the internal tide-induced energy flux deduced from the global 1/10° internal wave-resolving model STORMTIDE and from satellite altimetry both show such a clear tidal beam emanating from the seamount chain south of the Azores (Figure 1). Guided by these maps, 12 locations for hydrographic stations with a minimum duration of 36 hr were chosen to study the internal tide-induced energy flux along the tidal beam (Figure 1).

Here we use this in situ data to study the decay of the internal tide energy along the tidal beam in comparison with the satellite altimetry and high-resolution model output. This paper is structured as follows: In section 2, the datasets (in situ observations, satellite altimetry, and STORMTIDE model output) are introduced, and the methods to derive the energy fluxes and the energy dissipation from these as parameters for the energy budget are described. In section 3, we first discuss the spatial patterns observed in the energy fluxes, the influence of the spring-neap cycle, and the energy flux partition into modes. We then compare the vertically integrated fluxes obtained from the in situ observations, from the STORMTIDE model output, and from satellite altimetry and discuss the differences between the three datasets. A summary of the results and the conclusions are presented in section 4.
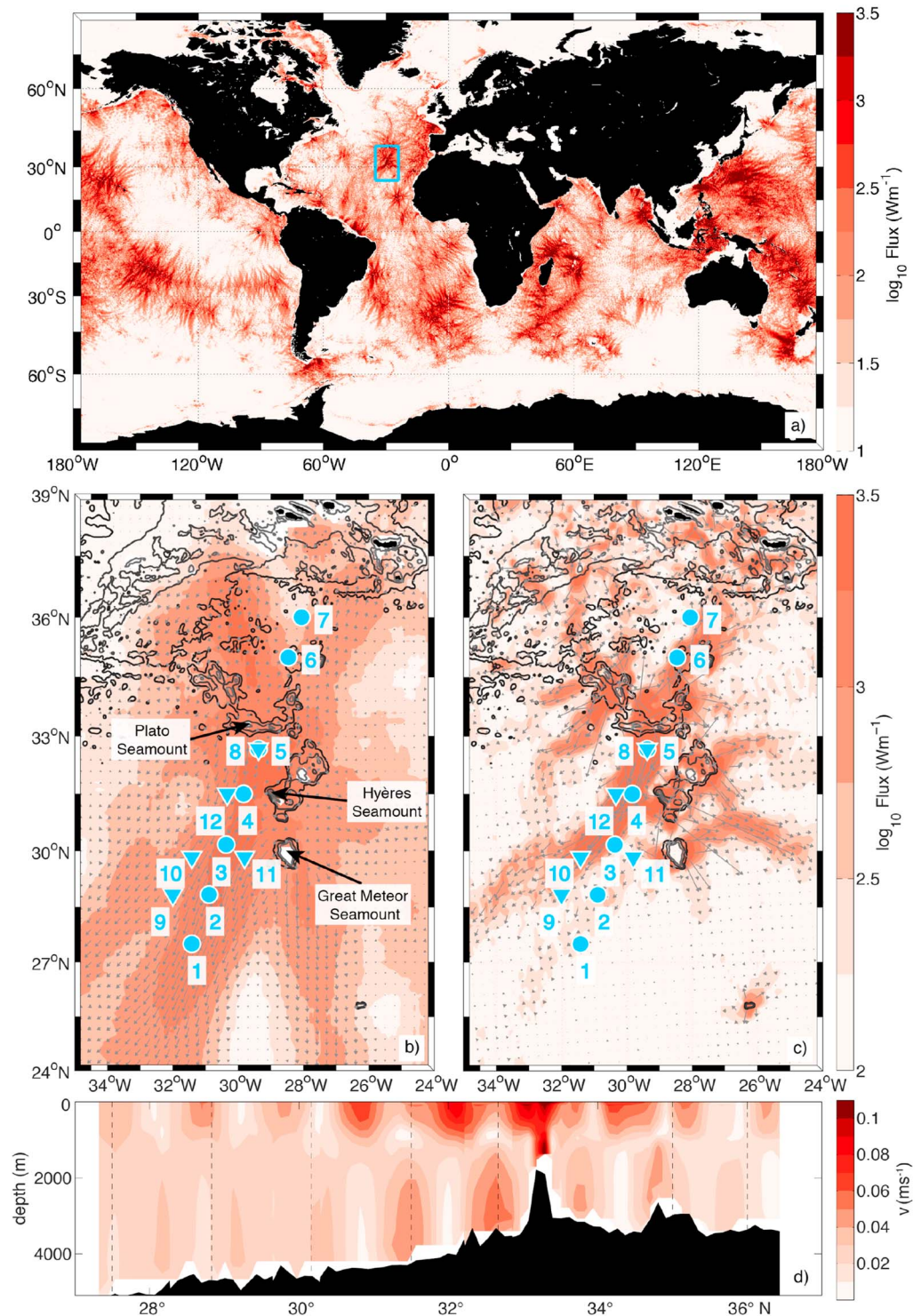
Figure 1. (a) Global map of M_2 internal tide energy flux in STORMTIDE; the blue rectangle denotes the measurement area. (b) and (c) show the positions of the 12 stations north and south of a seamount chain south of the Azores which induces a distinct internal tide beam. Circles denote stations carried out in August 2017 and triangles stations in May 2018. Vertically integrated M_2 energy fluxes from satellite altimetry (modes 1 and 2, (b)) and from STORMTIDE (c) are shown in color and gray arrows; topography is from ETOPO1 (Amante & Eakins, 2009) and shows the 650-, 2000-, and 3000-m isobaths. For the energy fluxes derived from satellite altimetry, only every third grid point and for the STORMTIDE energy fluxes every second grid point is plotted for clarity. Note the different color maps and color scales in panel (a) compared to panels (b) and (c). (d) Amplitude of the meridional internal M_2 tide component along the beam in STORMTIDE, vertical dashed lines denote positions of Stations 1 to 7, seafloor topography is from ETOPO1 (Amante & Eakins, 2009).

2. Data and Methods

2.1. STORMTIDE

The STORMTIDE simulation (Müller et al., 2012) is performed with the tripolar version of the Max Planck Institute Ocean Model (Jungclaus et al., 2006; Marsland et al., 2003), developed within the framework of the German consortium project STORM (Storch et al., 2012; von Storch et al., 2016). The horizontal resolution is 0.1°, with a grid spacing of about 10 km near the equator and about 5 km or smaller south of 60°. In the vertical, 40 unevenly distributed vertical layers are used, with nine of them in the first 100 m. The parameterization of mesoscale eddies following Gent and McWilliams (1990) is switched off, as the 0.1-degree model resolves most of mesoscale eddies. The dissipation due to subgridscale processes is represented by several parameterizations. To represent vertical mixing of tracers and momentum, a modified PP scheme (Pacanowski & Philander, 1981) is used. The scheme includes a wind mixing, a Richardson-number-dependent mixing, and a constant background diffusivity. The horizontal mixing of tracers is parameterized through a grid-size-dependent isopycnal diffusion (Redi, 1982), whose strength depends on the grid size and is weak at a resolution of 0.1°. The horizontal dissipation of momentum is parameterized by a biharmonic diffusion. In the STORMTIDE simulation, the parameters in these parameterizations are set to the values normally used in climate simulations without tides. No parameter tuning is carried out, due to heavy computational costs.

The STORMTIDE simulation is forced by the complete lunisolar tidal potential, as calculated from the instantaneous positions of the Sun and Moon (Müller et al., 2012), thereby taking implicitly hundreds of tidal constituents into consideration (Thomas et al., 2001). The self-attraction and loading effect is parameterized in the same way as in Thomas et al. (2001; see also equation 4 in Müller et al., 2014). The simulation is forced at the sea surface by daily climatological wind stresses with a 365-day cycle and a sea surface temperature (SST) and sea surface salinity (SSS) restoration toward the monthly climatological values (Steele et al., 2001). A 10-year simulation has been performed, and baroclinic tidal energy fluxes were calculated from the last 2 years of the simulation (Müller, 2013). These energy fluxes are considered in this paper.

2.2. Vertically Integrated Internal Tide Energy Flux From Satellite Altimetry

Using a two-dimensional plane wave fit method, the temporally and spatially coherent part of the sea surface height expression of modes 1 and 2 of the internal tide can be extracted from altimetric sea surface height data (Zhao, 2018; Zhao & Alford, 2009; Zhao et al., 2011; Zhao et al., 2016). The associated baroclinic pressure fluctuations can be inferred using normal modes and, using linear theory, the corresponding horizontal velocity can be deduced (appendix in Zhao et al., 2016). From these, the vertically integrated mode 1 and 2 internal tide energy fluxes can be calculated.

2.3. In Situ Observations

STORMTIDE and satellite altimetry both indicate the Great Meteor Seamount Chain south of the Azores as the source region for the energetic internal tides south of the Azores (Figures 1b and 1c). Repeated measurements of conductivity, temperature, and depth (CTD) and lowered acoustic Doppler current profiler (LADCP) were obtained at 12 stations along the resulting tidal beam. Seven of these stations were carried out in August 2017 during RV Poseidon cruise POS516, following the maximum internal tide energy flux seen in satellite altimetry. In May 2018, during RV Poseidon cruise POS523, one station close to Plato Seamount was repeated, and four stations at the flanks of the beam were added.

At each station, vertical CTD/LADCP profiles were continuously measured over time periods of 36 to 48 hr, resulting in 11 to 16 profiles per station (Table 1). Consecutive CTD/LADCP profiles at each station were treated as time series that resolve the semidiurnal tide as well as the inertial frequency (∼24 hr) at all depths.

Horizontal velocities were measured with two Teledyne RD Instruments 300-kHz Workhorse Monitor acoustic Doppler current profilers and stratification with an SBE 911plus CTD. At the southernmost station (Station 1), the velocity data are limited to the upper 3000 m due to the decreasing abundance of scatterers. The CTD profiles at this station reach to 5000 m. On Station 11, only seven profiles could be measured with the LADCP due to technical problems with the power supply during Casts 5 to 9.

CTD data with a vertical resolution of 1 dbar from both the downcast and upcast are used for the calculation of horizontal internal wave energy fluxes. For the horizontal velocities, the LADCP data were processed using the LDEO IX 13 software package (https://www.ldeo.columbia.edu/~ant/LADCP.html), resulting in a single combined up and down profile which was then interpolated to a 1-dbar resolution to match the CTD

Table 1
Station Number, Positions, Duration of Time Series, Number of Full Profiles, Phase Within the Spring-Neap Cycle (N (S) is Neap (Spring) Tide ±1.5 Days, 0 Denotes Stations Between Spring and Neap Tide), rms of Absolute Barotropic Tidal Velocity During the Measurement (Generation) Time, Absolute Vertically Integrated Energy Flux, Vertically Integrated Along- and Across-Beam Energy Flux, and Absolute Energy Flux that was Rescaled to Account for the Spring-Neap Cycle at Each Station

Station #	Latitude	Longitude	Duration (hr)	# of profiles	S/N cycle phase at meas. time	Barotr. tide at meas. (gen.) time (cm s^{-1})	Abs. flux (kW m^{-1})	Along-beam (kW m^{-1})	Across-beam (kW m^{-1})	Rescaled flux (kW m^{-1})
1	27° 30.0′N	31° 25.0′W	44	11[a]	N	1.2 (1.7)	2.2	−2.2	0.2	3.6
2	28° 50.0′N	30° 53.5′W	39	10	0	1.7 (1.7)	0.5	−0.5	0	0.8
3	30° 10.0′N	30° 20.0′W	39	11	0	2.3 (2.8)	5.9	−4.8	−3.4	6.0
4	31° 30.0′N	29° 50.0′W	36	12	S	2.8 (4.1)	2.3	−2.3	0.4	2.0
5	32° 40.0′N	29° 22.3′W	42	15	S	3.3 (4.5)	4.6	−4.6	−0.5	3.7
6	35° 0.0′N	28° 27.5′W	40	15	0	2.6 (4.1)	0.6	0.4	−0.5	—[c]
7	36° 0.0′N	28° 3.5′W	38	16	N	1.5 (2.4)	1.0	−0.9	−0.4	—[c]
8	32° 40.0′N	29° 22.5′W	33	11	N	1.0 (2.5)	2.0	−1.8	0.9	2.8
9	28° 50.0′N	32° 0.0′W	39	14	0	2.1 (2.0)	1.2	−0.9	−0.8	1.6
10	29° 50.0′N	31° 25.0′W	43	13	S	3.0 (3.4)	3.1	−2.4	−2.0	2.7
11	29° 50.0′N	29° 40.0′W	40	12[b]	S	3.8 (3.1)	1.7	−1.7	0.2	1.3
12	31° 30.0′N	30° 20.0′W	41	14	0	3.1 (3.4)	3.4	−3.3	0.9	3.9

Note. Stations 1–7 are from Poseidon cruise POS516 in 2017 and Stations 8–12 from cruise POS523 in 2018. [a]Eleven LADCP profiles (last casts discarded) and 10 CTD profiles (first two casts discarded). [b]Seven LADCP profiles and 12 CTD profiles. [c]Not rescaled due to unknown generation site.

data. To reduce the influences of small-scale processes and instrument noise in the LADCP data, CTD and LADCP profiles were 50-m low-pass-filtered for the calculation of vertically integrated energy fluxes (Polzin et al., 2002).

During POS523, microstructure profiles were measured in the upper 500 m with a Rockland VMP-250. Measurements were carried out in 2 hr ensembles between sets of CTD/LADCP deployments. Each ensemble consists of three to five casts, resulting in 8 to 17 microstructure profiles at each station. The microstructure measurements do not always fully resolve the tidal cycle, but there is no bias in the measurement times in relation to the tidal phase at any station.

2.4. Caveats in Combining In Situ Measurements, Satellite Altimetry, and STORMTIDE

The in situ measurements used in this study provide the most direct estimate of the internal tide energy flux but are subject to, for example, instrument restrictions and relatively short measurement durations that limit the accuracy with which the tidal signal can be extracted from the measured time series. Additionally, they provide pointwise information in both space and time and do not resolve temporal variability in direction and magnitude in the energy fluxes which can be challenging in a direct comparison with model- or altimetry-based energy fluxes (Chiswell, 2006). Part of the missing temporal information can potentially be addressed by applying a rescaling of the energy flux to take the spring-neap cycle into account (section 3.2).

STORMTIDE is capable of providing a description of full three-dimensional features of low-mode internal tides in a dynamically consistent manner (i.e., consistent within the primitive equations). However, it is driven by climatological winds and by restoring SST and SSS to climatological values. This may lead to unrealistic features, for instance, the restoring conditions will damp the fluctuations near the sea surface, and weaker mesoscale eddies may be expected. Moreover, the model does not resolve dissipation processes which have to be parameterized (see section 2.1). All these parameterizations can affect the dissipation of the simulated internal tides. It is not clear how the parameters should be tuned to take into account the mixing due to resolved internal waves. In addition, the model contains also numerical dissipation related to discretization. The strength of this dissipation and its effect on the simulated internal tides are unclear. Further investigations are needed to quantify the effects of parameterizations used on the dissipation of the resolved internal waves and eventually to improve the fidelity of the simulated internal waves.

Satellite altimetry gives a good estimate of the multiyear mean of the coherent part of the internal tide flux which in many areas is most likely a lower-bound estimate for the in situ fluxes. The data processing

additionally leads to a suppression of the east-west-oriented waves due to the generally north-south-oriented satellite tracks (de Lavergne et al., 2019; Zhao, 2018; Zhao et al., 2016), and the spatial resolution of the satellite-based energy fluxes is limited due to the spatial coverage of the satellites. Internal tide parameters from satellite altimetry are determined by fitting plane waves to time series of sea surface height in windows of 160 km × 160 km on a 0.1° × 0.1° grid. This results in a smoothed map of internal tide energy fluxes, while STORMTIDE includes patterns on smaller spatial scales. For parts of the discussion, STORMTIDE energy fluxes are filtered to mimic the spatial resolution of the altimetry-based energy fluxes (interpolation on a 0.1° × 0.1° grid and applying a 160 km moving average filter), thus making the modeled and satellite-based energy fluxes more comparable in the sense of resolved spatial details.

2.5. Energy Flux Calculation

Time series of vertical displacements ξ of isopycnals were calculated from CTD data as (e.g., Gerkema & van Haren, 2007)

$$\xi(z, t) = -\frac{b(z, t)}{\overline{N^2}(z)} \tag{1}$$

with buoyancy b defined as

$$b(z, t) = -g\frac{\rho(z, t) - \bar{\rho}(z)}{\rho_*} \tag{2}$$

with the gravitational constant g, density ρ, the time means of buoyancy frequency and density denoted by $\bar{N}$ and $\bar{\rho}$ and the vertical mean of $\bar{\rho}$ by ρ_*. In depth ranges of very weak stratification, N^2 was set to 2×10^{-7} s^{-1}. The internal wave-induced velocity component is determined by (Nash et al., 2005)

$$\mathbf{u}'(z, t) = \mathbf{u}(z, t) - \overline{\mathbf{u}}(z) - \overline{\mathbf{u}_0}(t), \tag{3}$$

where $\mathbf{u}(z, t)$ is the measured horizontal velocity, $\overline{\mathbf{u}}(z)$ is its time mean, and $\overline{\mathbf{u}_0}(t)$ is determined from the baroclinicity condition

$$\frac{1}{H}\int_{-H}^{0}\mathbf{u}'(z, t)\mathrm{d}z = 0. \tag{4}$$

Using time series of vertical displacements and u' the vertically integrated horizontal energy flux by internal waves is calculated as

$$\mathbf{F} = \int_{-H}^{0}\langle\mathbf{u}'p'\rangle\mathrm{d}z \tag{5}$$

with $\langle\rangle$ denoting the average over a wave period and pressure anomaly p' obtained from

$$p'(z, t) = p'(z_0, t) + \int_{z}^{0}\rho'(\hat{z}, t)g\mathrm{d}\hat{z} \tag{6}$$

and $\rho' = \rho_*/g\overline{N^2}(z)\xi(z, t)$ and the baroclinicity condition for the depth-averaged pressure perturbation

$$\frac{1}{H}\int_{-H}^{0}p'(z, t)\mathrm{d}z = 0. \tag{7}$$

The amplitude of the M_2 and inertial signals in the time series were determined using a least-squares fit of these frequencies to the time series of vertical displacements (equation 1) and the internal wave-induced velocity signal (equation 3). The temporal resolution of the time series does not allow the separation of the diurnal tide signal (frequency 1/23.93 hr) and the inertial frequency (1/22.23 to 1/28.29 hr depending on station). As the amplitude of the diurnal barotropic tide in the TPXO9 model (Egbert & Erofeeva, 2002) is on the order of 0.5 cm s^{-1} (and therefore is expected to only induce a weak diurnal internal tide), the inertial frequency instead of the diurnal tide frequency was used in the least-squares fit.

Fluctuations in vertical displacements and horizontal velocities are dominated by signals of the semidiurnal tide at all stations. Two example time series are shown in Figure 2. One was measured at 31° 30′N/29° 50′W (Station 4), approximately 180 km away from one of the main areas of baroclinic to barotropic tide energy
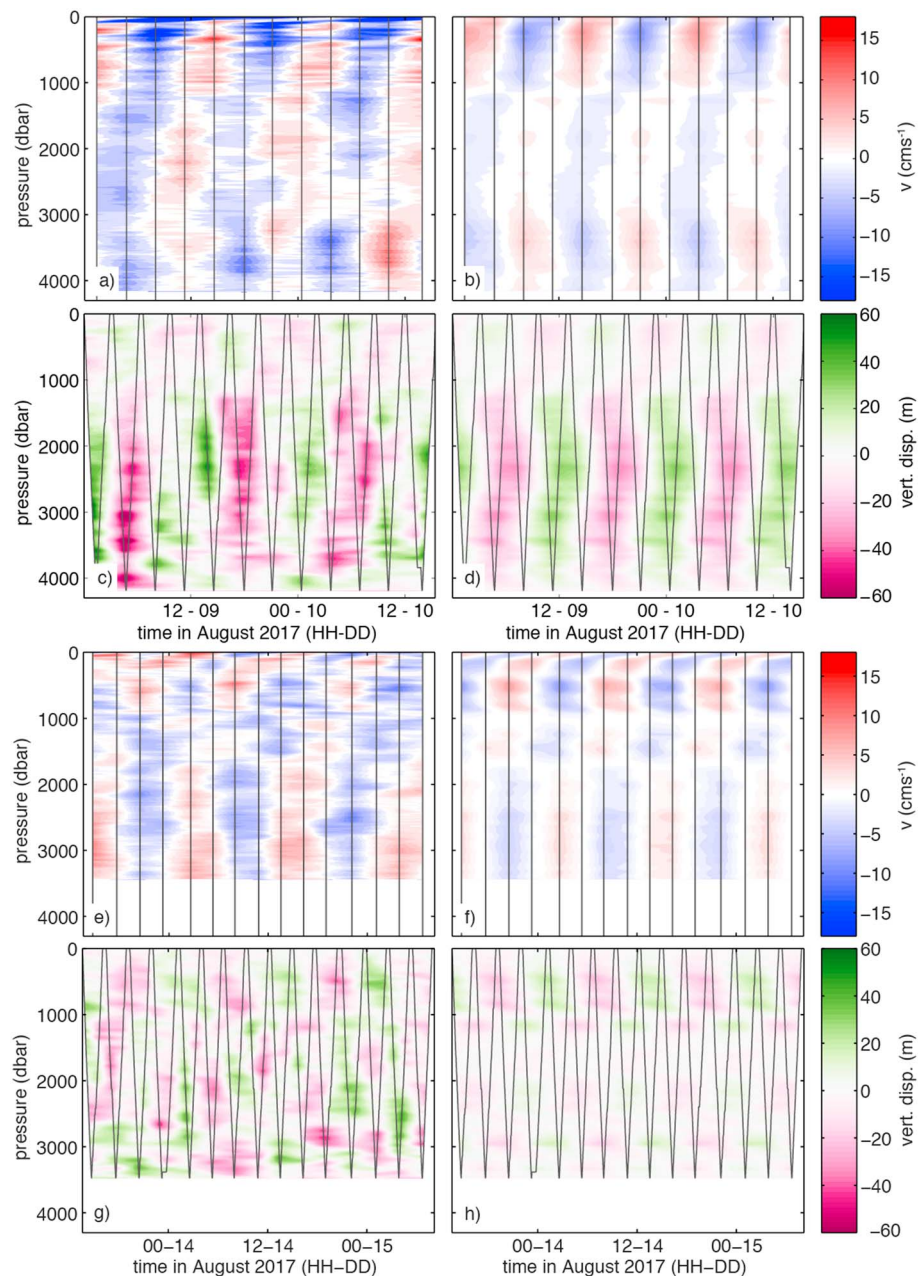
Figure 2. Example time series at 31° 30′ N/29° 50′ W (Station 4) and 35° 00′ N/28° 27.5′ W (Station 6) of total meridional velocity (a and e), its M_2 component (b and f), and corresponding plots for vertical displacements (c and g for the total signal and d and h for the M_2 component). Black lines denote individual profiles of CTD and velocity profiles, respectively.

conversion. A clear low-mode structure in both vertical displacements and horizontal velocity can be seen. At 35° 00′ N/28° 27.5′ W (Station 6), the vertical structure is more complex, indicating a larger energy flux in higher modes. At all stations, typical maximum amplitudes for internal M_2 tide signals in both horizontal velocity components lie between 5 and 15 cm s^{-1} with corresponding vertical displacement amplitudes of 20–40 m.

The energy flux was calculated from the full M_2 signal and for individual normal modes (modal structure was calculated using iModes; Haji, 2015): Horizontal velocity and vertical displacement data were least-squares fitted to the corresponding first five modes (e.g., Alford, 2003b; Nash et al., 2005) which were then used for calculating the energy flux in each of the modes using equation (5). These modal fits were also used to extend

the LADCP profiles at Station 1 from 3000 m and the CTD data from 4910 m (5000 dbar) to the seafloor at 5050 m.

For parts of the discussion, the zonal and meridional energy fluxes will be rotated into the along- and across-beam direction which is taken to be along the line formed by Stations 1 to 5 (direction of the tidal beam as seen in satellite altimetry).

2.6. Energy Dissipation From Finestructure Parameterization and Microstructure Measurements

Energy dissipation rates ε were computed on all stations from spectra of LADCP shear and CTD strain measurements using the finestructure parameterization of Gregg (1989) and Gregg et al. (2003), closely following the implementation of Kunze et al. (2006). This is an indirect method to estimate diapycnal diffusivities based on the theory of wave-wave interactions. In the finescale parameterization, the spectral energy transport rate in the vertical wavenumber domain is used to infer mixing intensities. It considers a signal at larger scales (internal waves) to infer diapycnal diffusivities by assuming that the spectral energy transport rate in the vertical wavenumber domain is proportional to the rate of turbulent production.

The finescale variances of shear $\langle V_z^2 \rangle$ and strain $\langle \xi_z^2 \rangle$ are determined from half-overlapping segments of 320 and 256 m length, respectively. Spectra are integrated with respect to vertical wavenumber as

$$\frac{\langle V_z^2 \rangle}{\bar{N}^2} = \int_{\min k_z}^{\max k_z} S[V_z^2/\bar{N}](k_z)\mathrm{d}k_z, \tag{8}$$

$$\langle \xi_z^2 \rangle = \int_{\min k_z}^{\max k_z} S[\xi_z^2](k_z)\mathrm{d}k_z \tag{9}$$

with the integration limits $_{\min}k_z = 1/320$ m^{-1} ($_{\min}k_z = 1/256$ m^{-1}) and $_{\max}k_z = 1/150$ m^{-1} ($_{\max}k_z = 1/10$ m^{-1}) for shear (strain), taking into account the different instrument noise and vertical structure of velocity and density.

Diapycnal diffusivity is computed from the strain variance as

$$K_\rho = K_0 \frac{\langle \xi_z^2 \rangle^2}{_{\mathrm{GM}}\langle \xi_z^2 \rangle^2} h(R_\omega) j\,(f/N)\,, \tag{10}$$

where $K_0 = 0.05 \times 10^{-4}$ m^2/s, N is the local buoyancy frequency, $_{\mathrm{GM}}\langle \xi_z^2 \rangle$ denotes the strain variance from the Garrett and Munk (GM) internal wave model (Gregg & Kunze, 1991; Munk, 1981), and f is the inertial frequency.

$$h(R_\omega) = \frac{1}{6\sqrt{2}} \frac{R_\omega(R_\omega + 1)}{\sqrt{R_\omega - 1}} \tag{11}$$

accounts for the frequency content of the internal wave field and depends on the ratio between shear and strain

$$R_\omega = \frac{\langle V_z^2 \rangle/_{\mathrm{GM}}\langle V_z^2 \rangle}{\langle \xi_z^2 \rangle/_{\mathrm{GM}}\langle \xi_z^2 \rangle} \times 3. \tag{12}$$

The in situ shear and strain variance values were normalized by the corresponding GM estimates in the respective wavenumber ranges to account for the different integration limits in the shear and strain spectra. The factor of 3 is the GM shear to strain variance ratio (Munk, 1981).

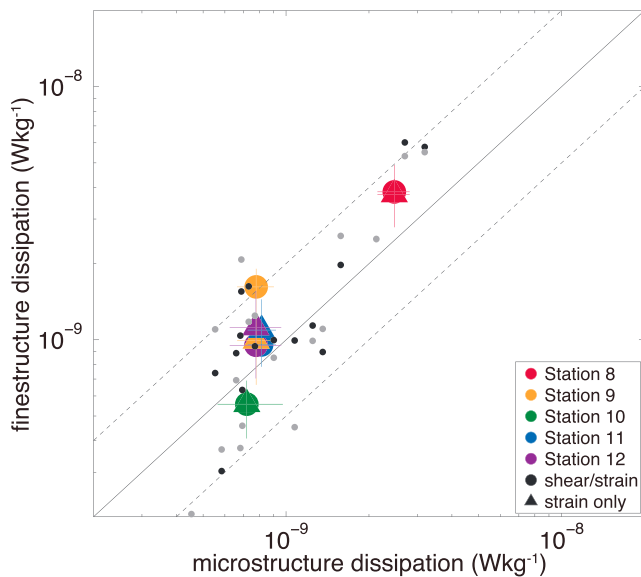The latitude dependence of the internal wave field is parameterized as

$$j(f/N) = \frac{f \, \mathrm{arccosh}(N/f)}{f_{30} \, \mathrm{arccosh}(N_0/f_{30})}, \tag{13}$$

where the terms $N_0 = 5.24 \times 10^{-3}$ rad/s and $f_{30} = f(30°)$ denote the reference buoyancy frequency and inertial frequency. Energy dissipation ε was determined from turbulent diffusivity using the Osborn (1980) relation

$$K_\rho = \Gamma \frac{\varepsilon}{N^2}, \tag{14}$$

assuming a mixing efficiency of $\Gamma = 0.2$.

The corresponding parameterization based on the shear variance can be expressed as
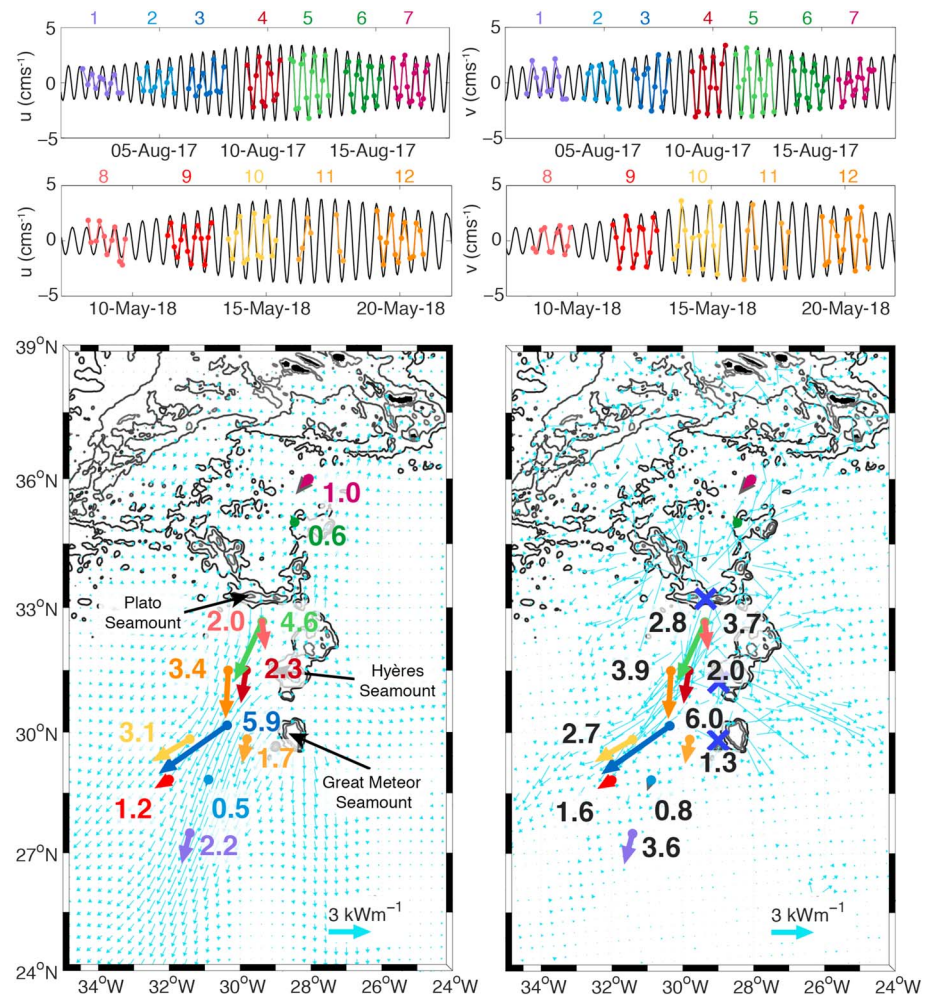
$$K_\rho = K_0 \frac{\langle V_z^2 \rangle^2}{{}_{GM}\langle V_z^2 \rangle^2} h_2(R_\omega) j\,(f/N) \tag{15}$$

with

$$h_2(R_\omega) = \frac{3(R_\omega + 1)}{2\sqrt{2}R_\omega\sqrt{R_\omega - 1}} \tag{16}$$

Energy dissipation rates ϵ were computed at all stations using the parameterization based on shear and strain and the strain-only parameterization with a fixed shear to strain ratio R_ω of 3 (the Garrett Munk shear/strain variance ratio). When the strain-only parameterization is applied, using a value of 3 for R_ω has been shown to yield energy dissipation rates that are in good agreement with corresponding values from microstructure measurements (Whalen et al., 2015). North of the Plato Seamount (Stations 6 and 7) in the depth range from 500 to 1500 m, the shear-based version of the parametrization was used ($R_\omega = 3$) because here intrusions of Mediterranean Water are observed (Zenk, 1970) that cause finescale signals in strain which are unrelated to internal waves. At the southernmost station (Station 1), the strain-only parametrization is applied below 3000 m because good-quality velocity data are missing.

To avoid mixed layer structures and wind-induced variability, dissipation rates were calculated starting at 200 m depth at all stations. Varying the integration limits for shear and/or strain (10 to 100 m or 100 to 250 m for strain and 50 to 150 m for shear) typically induces a spread in the resulting dissipation estimates on the order of 2. Using only the short wavelengths in the shear integration results in higher values (except at


Figure 3. Dissipation rates from finestructure parameterization based on shear and strain (circles) and from the strain-only parameterization (triangles) compared to dissipation rates from microstructure measurements at the five stations carried out in 2018. Confidence intervals were determined by 90% bootstrapping. Small circles denote comparisons between mean dissipation rates in each individual microstructure ensembles in comparison to the mean dissipation rate from finestructure from the hydrographic profiles directly before and after the respective microstructure ensemble. Black denotes shear- and strain-based solutions and gray strain-only. Dashed lines denote an agreement within a factor of 2.

Station 3), which is probably due to the higher noise level in the LADCP data at smaller scales. There is no clear systematic deviation between short and long wavelength limits in the strain-only parameterization (four estimates are higher when only the long wavelengths are considered; eight estimates are lower). Estimates based on the short wavelengths are closer to those based on the full integration range (10 to 250 m) as on short scales strain is higher than in the long wavelength range (100 to 250 m) and thus dominates the integral over the full (10 to 250 m) integration range.

Mean dissipation rates from the microstructure profiles measured at each of the stations during the 2018 cruise (between 8 and 17 per position) were used for comparisons with the two finestructure-based estimates (shear- and strain-based and strain-based with a fixed R_ω) at the respective stations in the depth range from 200 m to the maximum depths of the microstructure profiles of about 500 m. This approximately coincides with the depth range covered by the first finestructure segment (200–520 m). In this depth range, the mean dissipation rates derived from the microstructure measurements as well as the two finestructure parameterizations are in good agreement (Figure 3). The highest deviation between the finestructure estimates based on shear and strain and the strain-only estimates as well as the maximum difference between the two finestructure-based estimates and the energy dissipation rates from the microstructure measurements is less than a factor of 2 (Figure 3). When mean dissipation rates from individual microstructure ensembles (three to five profiles) are compared to the mean dissipation rates from the finestructure parameterization of the respective adjacent hydrographic profiles (gray dots in Figure 3), for both the shear- and strain-based and the strain-only parameterization, only 3 out of 17 ensembles deviate by more than a factor of 2. We do not expect a significant impact of the temporal resolution of the microstructure measurements on this result as there is no systematic bias in the measurement times in relation to the tidal phase at any station. Further, the data do not indicate a dependence of the energy dissipation rate on the tidal phase. This is in agreement with findings in the upper water column of Klymak et al. (2008) who argue that the time scale for the energy cascade from large to small scales (following the Gregg-Henyey model) is on the order of the spring-neap cycle, rendering a direct correlation with the tidal phase improbable.

Figure 4. (top four panels) Barotropic velocities at the stations along with the TPXO9 (Egbert & Erofeeva, 2002) prediction in black. (bottom left and right) Vertically integrated M_2 internal tide energy fluxes in kilowatts per meter at 12 stations along the tidal beam as colored vectors and numbers; gray numbers on the right panel are energy fluxes rescaled accounting for the spring-neap cycle using equation (17). Topography in the background (650, 2000, and 3000 m isolines) is from ETOPO1 (Amante & Eakins, 2009), blue crosses denote positions of generation sites used for the spring-neap scaling, and M_2 energy fluxes from satellite altimetry (modes 1 and 2, left) and from STORMTIDE (right) are shown as light blue arrows. For the energy fluxes derived from satellite altimetry, only every third vector and for the STORMTIDE energy fluxes every second vector is plotted for clarity.

3. Energy Fluxes Along the Tidal Beam

3.1. Spatial Pattern of Energy Fluxes From In Situ Data

At the 12 stations during the two cruises, the observed vertically integrated energy fluxes follow the general direction predicted by STORMTIDE and seen in satellite altimetry (Figure 4). They reach magnitudes of roughly $1\,\mathrm{kW\,m^{-1}}$ between the Plato Seamount and the Azores and more than $5\,\mathrm{kW\,m^{-1}}$ close to the internal tide-generating seamounts. The absolute tidal energy flux is dominated by the along-beam fluxes, while the across-beam fluxes are weaker (Figure 4 and Table 1).

Directly south of the east-west-oriented Plato Seamount that stands out as a main generation site of internal tides in STORMTIDE and in satellite altimetry, two time series (Stations 5 and 8) were measured at the same position. One was obtained during spring tide (2017) and the other during neap (2018, see Figure 4, top panel). Close to the generation site, the spring-neap cycle induces a factor of about 2.5 difference in the observed absolute energy flux and in the along-beam energy flux component between spring (Station 5) and neap (Station 8) phases (Table 1). The across-beam component is small during both phases (0.5–$0.9\,\mathrm{kW\,m^{-1}}$) but changes its direction from westward during spring phase to eastward during neap phase.
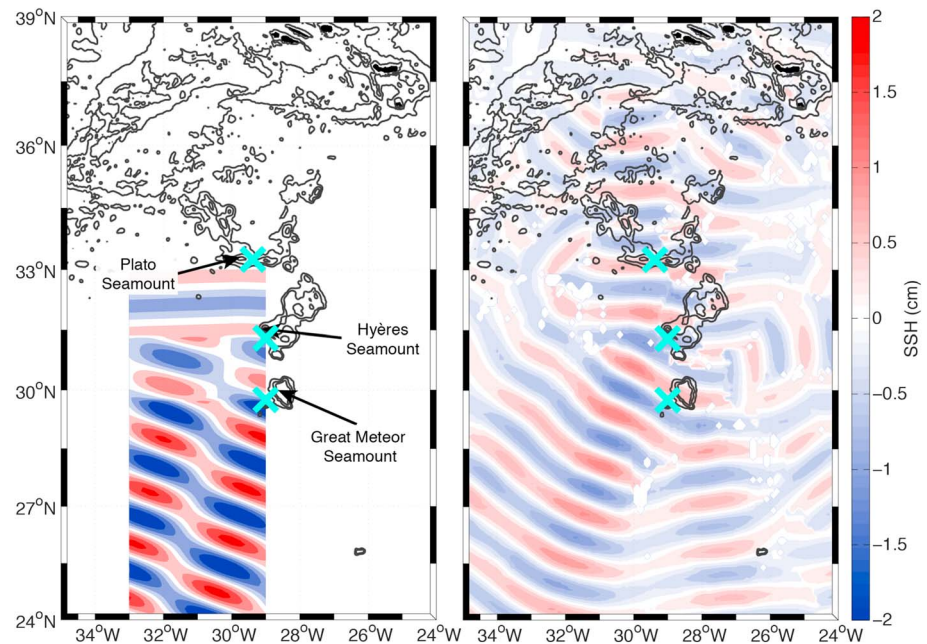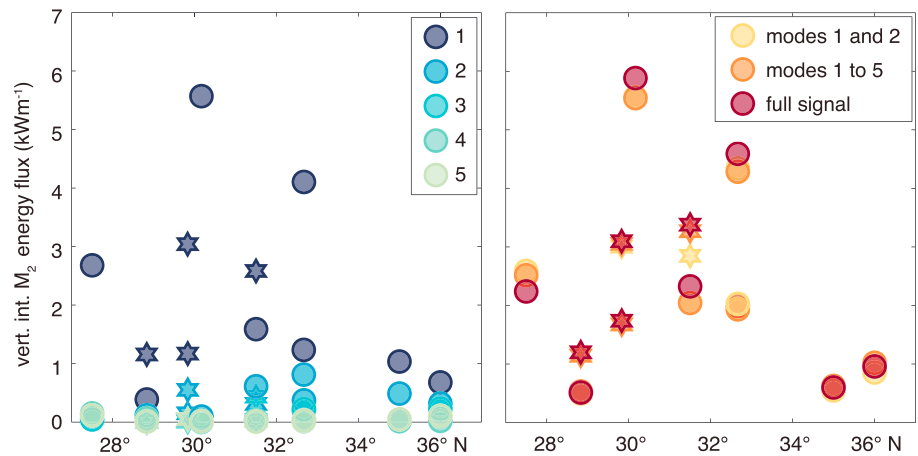
Figure 5. (left) Sea surface height (SSH) signal of the interference pattern formed by plane waves generated at the three main generation sites (Plato, Hyères, and Great Meteor Seamounts, denoted by cyan crosses). (right) Full SSH pattern of the most energetic mode-1 waves as deduced from satellite altimetry.

Moving south, the along-track energy flux decreases compared to its spring-tide value close to the generation site, and a zonal change of 1 kW m^{-1} is observed between the neighboring Stations 4 and 12 (distance 45 km). West of the Great Meteor Seamount (Stations 3, 10, and 11), both the along- and across-beam energy fluxes in the center of the beam (Station 3) strongly increase, probably due to an additional flux originating from the Great Meteor or Hyères Seamount to the East (Figure 4). Toward the flanks of the beam, the energy flux decreases by about a factor of 2 (Station 10) and 3.5 (Station 11) over a distance of O(100 km). A similar pattern is seen in satellite altimetry (Figure 4, bottom left). On the southern flank of the Great Meteor Seamount, outside of the main tidal beam, Gerkema and van Haren (2007) found an energy flux of 2.3 kW m^{-1} away from the seamount which is similar to the flux magnitudes found in this study along the flanks of the tidal beam.

Stations 2 and 9 are located at 29° N, the critical latitude for PSI that in theory can transfer internal M$_2$ tidal energy to subharmonics by nonlinear wave-wave interactions (i.e., at the positions of Stations 2 and 9 to the inertial period). Here the along-track tidal energy flux decreases to approximately 1 kW m^{-1}, while an increase by about a factor of 2 in the inertial energy flux at Stations 1–3 (27° 30.0′ N to 30° 10.0′ N) compared to the more northward stations is found (not shown). No corresponding decrease in the internal tide energy flux is seen in STORMTIDE or satellite altimetry. As PSI would result in a loss of energy in the coherent part of the internal tidal signal (which is seen by satellite altimetry), a decrease in the satellite altimetry-based energy fluxes would be expected in case of an average decrease in the magnitude of internal tides at or equatorward of the critical latitude. Effects like the Doppler shifting of the tidal frequency by the mean currents (Richet et al., 2017), the long time scales involved in wave-wave interactions which are in general large compared to the wave periods (Eden et al., 2019) and the limited spatial resolution of the in situ observations restrict the detectability of PSI-related effects. Thus, similar to previous studies (Alford & Zhao, 2007b; Carter & Gregg, 2006; Kunze, 2017; MacKinnon et al., 2012), we cannot make conclusive statements on the significance of PSI-related effects for the propagation of low-mode internal tides in our study area.

At the southernmost station, the energy flux increases again to 2.2 kW m^{-1}, similar to what is observed north of the critical latitude at Station 11. Between the Plato Seamount and the Azores, only weak tidal energy fluxes are observed (Stations 6 and 7). A change in the flux direction between these two stations from northeastward (away from Plato Seamount, Station 6) to southwestward (toward the seamount, Station 7) indicates additional internal tides originating from the Azores islands propagating southward.

Figure 6. Energy flux distribution over mode 1 to 5 (left) and their sum in comparison to the full energy flux (right). Circles denote Stations 1 to 8 in the center of the tidal beam; stars denote off-beam Stations 9–12.

3.2. Interference Pattern and Spring-Neap Cycle

From the energy flux pattern seen in satellite altimetry, STORMTIDE, and in situ measurements, the Plato, Hyères, and Great Meteor Seamounts appear to be the main generation sites for the internal tides that form the internal tide beam. To test this assumption, an interference pattern formed by plane waves originating at these three seamounts was constructed. The sea surface height (SSH) amplitude, direction, and phase of the most energetic mode 1 wave as deduced from satellite altimetry at the three seamounts are used as initial properties of the waves. As these waves are directed toward the South/Southwest, the SSH pattern between the Plato and Hyères Seamounts shown in Figure 5 is formed only by the wave generated at the Plato Seamount. Between the Hyères and Great Meteor Seamounts, it is the sum of the Plato and Hyères waves, and south of the Great Meteor Seamount, it is the combination of all three waves. The exact structure of the interference pattern is sensitive to the exact phases and directions of the three waves, but the general beam structure and direction is relatively robust. The resulting interference pattern is qualitatively similar to the full pattern of the internal tide SSH signal derived from altimetry (Figure 5) and supports the three seamounts as dominant generation sites.

The internal tide energy flux is proportional to the square of the amplitude of the barotropic tide at its generation site and time (St. Laurent & Garrett, 2002). When the exact generation locations of the internal tides is known, the in situ internal tide energy fluxes can be rescaled to account for the different measurement times within the spring-neap cycle. The rescaled fluxes F_s are calculated as

$$F_s = F(t)[u_{bt}(t)/u_{bt}^{ref}]^2 \tag{17}$$

(Alford et al., 2011), where $F(t)$ is the internal tide energy flux from the in situ measurements, $u_{bt}(t)$ is the barotropic tide from TPXO9 (Egbert & Erofeeva, 2002; which is in very good agreement with the barotropic tide deduced from the in situ measurements, see top panels in Figure 4) at the time of the internal tide generation, and u_{bt}^{ref} is the root-mean-square amplitude of the barotropic tide during the two cruises at the respective generation sites. To calculate the amplitude of the barotropic tide at the generation time of the observed internal tides, the time it takes for the internal tides to propagate from their sources to the measurement location needs to be estimated. As the dominant energy flux direction is southward, for each in situ station, the seamount that is closest to its north is assumed as dominant generation site (Plato Seamount for Stations 4, 5, 8, and 12; Hyères Seamount for Stations 3, 10, and 11; and Meteor Seamount for Stations 1, 2, and 9). A propagation speed of 2.3 m s^{-1} (mean propagation speed of a mode-1 wave at the in situ stations) is assumed for the calculation of the time lag between the time of the generation of the internal tide and the time of the measurement. No scaling is done for the stations north of the Plato Seamount as no distinct generation site for the observed internal tides can be determined.

Close to the Plato Seamount, the scaling of the in situ fluxes that were measured at the same position but at opposite maxima of the spring-neap cycle (Stations 5 and 8) results in values that are in closer agreement (2.8 and 3.7 kW m^{-1} compared to 2.0 and 4.6 kW m^{-1} without scaling). At the southernmost station (Station 1),
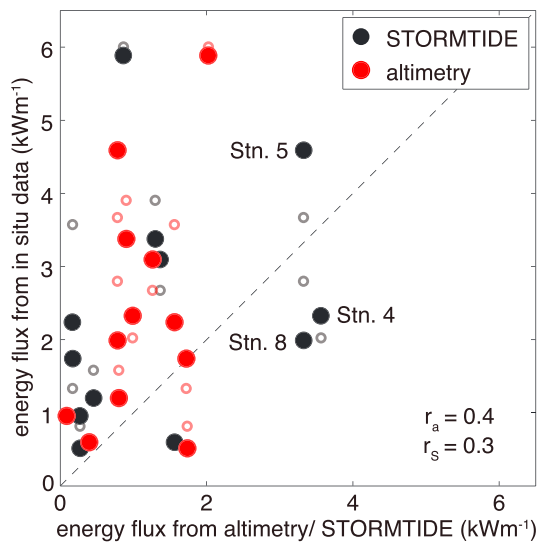
Figure 7. Comparison of vertically integrated internal tide energy fluxes from in situ measurements and from satellite altimetry (red) or STORMTIDE (black), a corresponding comparison with the in situ flux estimates that were rescaled to account for the spring-neap cycle is shown as open circles. The dashed black line denotes a one-to-one relation, correlation coefficients are given by r_S for the correlation between estimates from in situ measurements and estimates from STORMTIDE and by r_a for the comparison with estimates based on satellite altimetry.

the energy flux is considerably enhanced by the scaling (3.6 kW m^{-1} compared to 2.2 kW m^{-1}) as the station was carried out during a neap phase and the close-by Meteor Seamount was assumed as dominant generation site. This simple assumption probably overestimates the effect of the spring-neap cycle as the flux measured at this position will be the result of the interference of waves from (at least) the Plato, Hyères, and Meteor Seamounts which results in a less clear correlation with the spring-neap cycle (and thus a rescaling factor closer to 1) due to the different propagation times. The remaining in situ measurements were carried out in phases of the spring-neap cycle during which the barotropic tide was close to its mean values; thus, the scaled values do not strongly differ from the unscaled values.

### 3.3. Modal Partitioning of Energy Fluxes

M_2 internal tide signals in horizontal velocities and in vertical displacements were fitted to the first five vertical normal modes, and the corresponding vertically integrated energy flux in each mode was calculated from equation (5). The majority of the measured energy flux is contained in the first mode (Figure 6). A higher percentage of energy in higher modes is found in the center of the tidal beam at the critical latitude (Station 2), as well as between the seamounts and the Azores (Station 7), where in both cases, at least 10% of the energy flux is contained in modes 3–5. During neap phase, the energy flux in higher modes increases close to the Plato Seamount north of Station 8 with slightly more than 10% of the entire energy flux contained in modes 3 to 5. Off the center of the beam, at Station 12, the energy in higher modes also increases with about 15% in modes 3 to 5.

In agreement with the in situ observations, a shift in the modal content of the energy flux close to the Plato Seamount (position of Stations 5 and 8) and between the seamount and the Azores (position of Station 7) is also found in satellite altimetry (not shown). While away from these sites only a small fraction of the energy flux is contained in mode 2 compared to mode 1 (less than 3%), the percentage increases to 18% at the position of Stations 5/8 and to 12% at the position of Station 7. When comparing the in situ energy flux calculated from the full tidal signals (not fitted to normal modes) at each station to the corresponding sum of the in situ energy fluxes contained in modes 1 and 2 and in modes 1 to 5, the maximum deviation is 16 % and 12%, respectively (Figure 6, right). These results are in agreement with findings of Alford et al. (2011) in the Luzon Strait and Vic et al. (2018) who showed that even though the major part of the energy converted into internal tides over the Mid-Atlantic Ridge is contained in higher modes, the energy flux is dominated by the first mode.

The concentration of the energy flux in the first two modes within the tidal beam implies that, if these modes can be resolved (as they are in STORMTIDE and satellite altimetry), the majority of the flux within internal tide hot spots can, in principle, be adequately captured.

3.4. Comparison of In Situ Measurements, Satellite Altimetry, and STORMTIDE

A pointwise comparison of the vertically integrated internal tide energy fluxes from in situ measurements with satellite altimetry and STORMTIDE shows correlation coefficients of 0.4 and 0.3, respectively (Figure 7). Using the energy fluxes that are rescaled regarding the spring-neap cycle (except Stations 6 and 7 where the unscaled values are used; cf. section 3.2) gives corresponding correlations coefficients of 0.2 and 0.4. Due to the large scatter in the data and the limited number of observations, none of the correlation coefficients are significant at the 85% level. Overall, the internal tide energy fluxes from the in situ measurements are higher than both the corresponding estimates from STORMTIDE and especially than the altimetry-based estimates. In STORMTIDE, higher energy fluxes are found close to the internal tide-generating Plato Seamount (Stations 4, 5, and 8) which are not present in the altimetry. This is representative for the overall higher maximum energy flux values in STORMTIDE compared to the altimetry-based estimates.
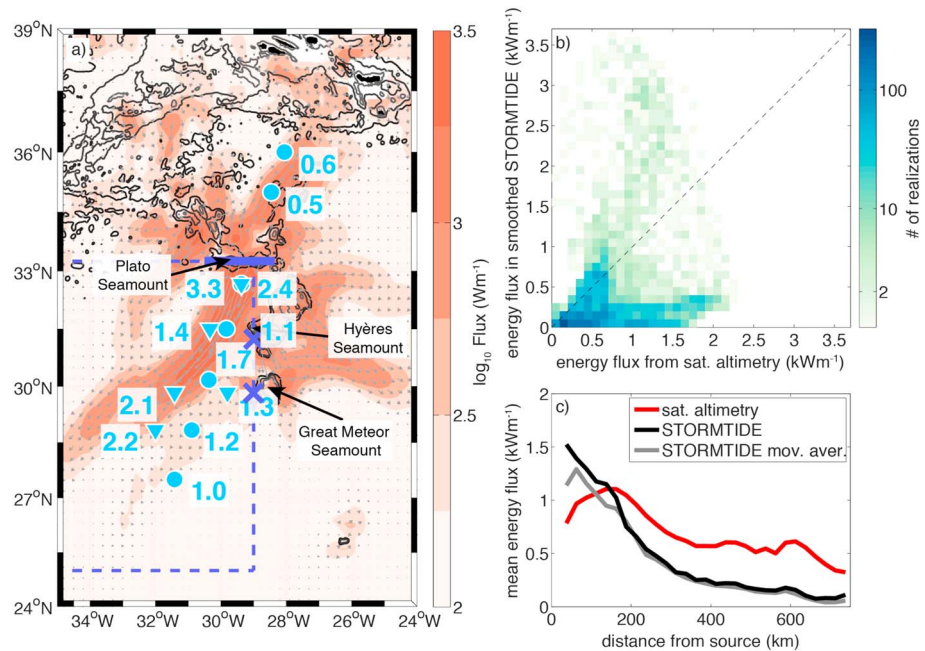
Figure 8. (a) Blue numbers give mean vertically integrated energy dissipation rates (in mW m^{-2}) from the strain-only finestructure parameterization at the 12 stations with smoothed STORMTIDE internal tide energy fluxes in the background (only every third vector is plotted for clarity). The blue line and crosses denote the main internal tide generation sites; the dashed box shows the area used for the right panels. (b) 2-D histogram of internal tide energy fluxes from satellite altimetry and the smoothed STORMTIDE data set, note the logarithmic color scale. The dashed line denotes the one-to-one relation. (c) Mean internal tide energy flux against distance from the closest of the three source regions from satellite altimetry (red), in STORMTIDE (black), and the smoothed STORMTIDE data (gray).

Filtering of the STORMTIDE energy fluxes to mimic the spatial resolution of the altimetry-based energy fluxes (interpolation on a 0.1° × 0.1° grid and applying a 160 km moving average filter; cf. section 2.4) results in comparable spatial details as in the altimetry-based maps (Figure 8) and decreases the maximum flux values. This indicates that the limited spatial resolution of the altimetry-based fluxes potentially is one of the main reasons (next to, e.g., the long-term smoothing) for the overall lower maximum flux values compared to the in situ observations and to STORMTIDE. A visual comparison with Figure 1b shows that while in the smoothed STORMTIDE dataset, the magnitude of the internal tide flux close to the main generation sites is similar to that derived from altimetry, the energy decrease with increasing distance to the generation sites is much stronger.

A 2-D histogram of internal tide energy flux magnitudes from satellite altimetry and in the smoothed STORMTIDE data in the area of the tidal beam southwest of the Plato Seamount (dashed box in Figure 8a) shows that while at some positions (which are close to the main generation site), the energy flux in STORMTIDE exceeds the corresponding estimates from altimetry, the majority of energy flux values in STORMTIDE is lower than those from altimetry (Figure 8b). This indicates a faster energy dissipation in the model compared to what is seen in altimetry.

To qualitatively compare the long-range propagation of the internal tides in STORMTIDE and altimetry, mean energy fluxes versus distance from the generation sites were calculated in both data sets (Figure 8c). As for the spring-neap-cycle discussion, it is assumed that the respective closest seamount north of the considered grid point is the (main) generation site and is therefore used as source for the distance calculation. Similar to the pointwise comparison, the mean energy flux close to the generation sites is higher in STORMTIDE, while the decrease of the mean energy flux with increasing distance is stronger than for the altimetry. In the model, the mean energy flux decreases by approximately 1 kW m^{-1} over 300 km which is equivalent to an energy dissipation of roughly 3 mW m^{-2} (not taking additional energy conversion along the propagation path into account).

Estimates of the vertically integrated energy dissipation rates at the 12 in situ stations from the strain-based finestructure parameterization range from 0.5 to 3.3 mW m^{-2} with the highest dissipation rate at the station closest to the Plato Seamount and the lowest values at the two northernmost stations between the Plato Seamount and the Azores (Figure 8). At the two southernmost stations within the tidal beam but away from the generation sites, the energy dissipation rate is approximately 1 mW m^{-2} which is in good agreement with what was observed for low-mode internal tides in the Tasman Sea (Waterhouse et al., 2018).

The spatial pattern in the corresponding energy dissipation rates from the parameterization based on shear and strain (not shown) is less clear. The most noticeable differences between individual vertically integrated energy dissipation rates from shear and strain compared to the strain-only parameterization are found at Stations 9 and 11 (factors of 2 and 3, respectively) which were carried out in 2018. Here discrete layers of high near-inertial shear at large vertical wavenumbers lead to high energy dissipation rates in individual segments of the shear- and strain-based finestructure parameterization. Potential sources of the enhanced small-scale near-inertial shear and the resulting higher energy dissipation rates could be the stronger winds during the cruise in 2018 compared to the cruise in 2017, scattering of internal waves by interactions with background currents or wave-wave interactions.

The overall lower and spatially more coherent strain-only estimates are in good agreement with the long-range internal tide propagation seen in satellite altimetry, and the area south of the Azores generally is an area of weak winds and background currents. Thus, we consider the strain-only estimates, which are less sensitive to the (likely infrequent) small-scale near-inertial waves, to be more representative for the mean energy dissipation along the beam.

The relatively low energy dissipation rates and the correspondingly weak decrease in the in situ energy fluxes away from the source regions are in agreement with the expected weak topographic scattering of low-mode waves. As discussed in St. Laurent and Garrett (2002), low modes can travel O(1000 km) before scattering from topography, and much of the internal tide energy is conserved during each individual bottom encounter. An additional energy loss from the internal tide will be induced by wave-wave interactions. Even though south of 29° N, the M$_2$ tidal frequency falls into the frequency range $2f < \omega_0 \leq 3f$, the frequency range where Eden et al. (2019) find the predominant energy loss due to wave-wave interactions, these occur on time scales longer than the wave periods. They will thus also not result in high energy dissipation rates and low-mode internal tides can propagate far away from their generation sites.

4. Summary and Conclusions

A distinct internal tide beam originating from a group of seamounts south of the Azores is studied in three independent data sets: the global low-mode internal wave-resolving STORMTIDE model, satellite-derived mode-1 and mode-2 internal tide energy fluxes, and internal tide energy fluxes calculated from in situ stations. Main internal tide generation sites that contribute to the resulting flux pattern are the Plato, Hyères, and Meteor Seamounts where vertically integrated internal tide energy fluxes based on in situ measurements reach amplitudes of 5–6 kW m^{-1}. Along the beam and with increasing distance to the generations sites, the in situ energy fluxes decrease nonmonotonically to approximately 1 kW m^{-1}. Crossing the critical latitude for PSI, we see a drop in internal tide energy flux with a concurrent increase in the inertial signal, but the spatial resolution of the in situ measurements is not sufficient to make any statements about PSI-related processes.

The in situ observations show that even close to the main internal tide generation sites, the energy flux can primarily be contained in the first mode. This is in agreement with observations close to Hawaii (Lee et al., 2006; Nash et al., 2006) and results of Vic et al. (2019) who also identify the seamount group south of the Azores as a prominent source of mode-1 waves. When only the energy flux in modes 1 and 2 is considered, at minimum 84% of the flux calculated from the full profile is captured. This shows that global models resolving the first two modes are generally able to capture the main characteristics of internal tide-induced energy fluxes for topography on scales typical for seamounts. For internal tide potential and kinetic energy and other topographic features such as wide ridge systems, higher modes might need to be resolved to adequately capture the internal tide field (Vic et al., 2018, 2019).

A direct comparison of the energy fluxes derived from the three different data sets shows that the in situ fluxes are generally higher than the corresponding fluxes in STORMTIDE and the energy fluxes derived

from altimetry. STORMTIDE resolves a lot of small-scale structure in the energy flux distribution, but high energy fluxes are restricted to locations close to the main generation sites. A qualitative comparison of the decrease of the energy flux away from the generation sites in STORMTIDE and altimetry shows that while the energy fluxes close to the sources are higher in STORMTIDE, the energy is quickly dissipated. This is not consistent with the energy dissipation rates derived from the finestructure parameterization away from the main generation sites (1 mW m^{-2}), and less dampening of the internal wave energy would improve the realistic representation of the life cycle of internal tides in global ocean models. The long-range propagation of the internal tides that is seen in altimetry seems to be more realistic, although the energy fluxes only include the coherent part of the internal tides and the spatial resolution of the energy fluxes is limited and thus does not resolve the maximum energy flux values close to the generation sites.

Overall, the in situ measurements confirm the internal tide pattern around the seamount chain south of the Azores as derived from satellite altimetry but are more variable and show a less monotonic decrease in the energy flux along the beam. Internal tides in STORMTIDE propagate over shorter distances compared to results from altimetry and in situ measurements, but the model resolves more spatial details close the main generation sites. The complexity of the interference pattern of internal tides generated by the multiple sources as well as the different approaches and limitations underlying the individual data sets make a more quantitative comparison extremely difficult. To foster the understanding of the generation, propagation, interaction, and dissipation of internal tides especially in more topographically and hydrographically complex settings, further observational studies are needed.

References

Alford, M. H. (2003a). Redistribution of energy available for ocean mixing by long-range propagation of internal waves. *Nature*, *423*, 159–162.

Alford, M. H. (2003b). Improved global maps and 54-year history of wind-work on ocean inertial motions. *Geophysical Research Letters*, *30*(8), 1424. https://doi.org/10.1029/2002GL016614

Alford, M. H., MacKinnon, J. A., Nash, J. D., Simmons, H., Pickering, A., Klymak, J. M., et al. (2011). Energy flux and dissipation in Luzon Strait: Two tales of two ridges. *Journal of Physical Oceanography*, *41*(11), 2211–2222.

Alford, M. H., Peacock, T., MacKinnon, J. A., Nash, J. D., Buijsman, M. C., Centuroni, L. R., et al. (2015). The formation and fate of internal waves in the South China Sea. *Nature*, *521*(7550), 65–69.

Alford, M. H., & Zhao, Z. (2007a). Global patterns of low-mode internal-wave propagation. Part II: Group velocity. *Journal of Physical Oceanography*, *37*(7), 1849–1858.

Alford, M. H., & Zhao, Z. (2007b). Global patterns of low-mode internal-wave propagation. Part I: Energy and energy flux. *Journal of Physical Oceanography*, *37*(7), 1829–1848.

Amante, C., & Eakins, B. W. (2009). ETOPO1 arc-minute global relief model: Procedures, data sources and analysis, (NOAA Technical Memorandum NESDIS NGDC-24). National Geophysical Data Center, NOAA. https://doi.org/10.7289/V5C8276M

Arbic, B. K., Richman, J. G., Shriver, J. F., Timko, P. G., Metzger, E. J., & Wallcraft, A. J. (2012). Global modeling of internal tides within an eddying ocean general circulation model. *Oceanography*, *25*(2), 20–29.

Arbic, B. K., Wallcraft, A. J., & Metzger, E. J. (2010). Concurrent simulation of the eddying general circulation and tides in a global ocean model. *Ocean Modelling*, *32*(3), 175–187.

Carter, G. S., & Gregg, M. C. (2006). Persistent near-diurnal internal waves observed above a site of M$_2$ barotropic-to-baroclinic conversion. *Journal of Physical Oceanography*, *36*(6), 1136–1147.

Chiswell, S. M. (2006). Altimeter and current meter observations of internal tides: Do they agree? *Journal of Physical Oceanography*, *36*(9), 1860–1872.

Clément, L., Frajka-Williams, E., Sheen, K. L., Brearley, J. A., & Garabato, A. C. N. (2016). Generation of internal waves by eddies impinging on the western boundary of the North Atlantic. *Journal of Physical Oceanography*, *46*(4), 1067–1079.

de Lavergne, C., Falahat, S., Madec, G., Roquet, F., Nycander, J., & Vic, C. (2019). Toward global maps of internal tide energy sinks. *Ocean Modelling*, *137*, 52–75.

Eden, C., & Olbers, D. (2014). An energy compartment model for propagation, nonlinear interaction, and dissipation of internal gravity waves. *Journal of Physical Oceanography*, *44*(8), 2093–2106.

Eden, C., Pollmann, F., & Olbers, D. (2019). Numerical evaluation of energy transfers in internal gravity wave spectra of the ocean. *Journal of Physical Oceanography*, *49*(3), 737–749.

Egbert, G. D., & Erofeeva, S. Y. (2002). Efficient inverse modeling of barotropic ocean tides. *Journal of Atmospheric and Oceanic Technology*, *19*(2), 183–204.

Falahat, S., Nycander, J., Roquet, F., & Zarroug, M. (2014). Global calculation of tidal energy conversion into vertical normal modes. *Journal of Physical Oceanography*, *44*(12), 3225–3244. https://doi.org/10.1175/JPO-D-14-0002.1

Gent, P. R., & McWilliams, J. C. (1990). Isopycnal mixing in ocean circulation models. *Journal of Physical Oceanography*, *20*(1), 150–155.

Gerkema, T., & van Haren, H. (2007). Internal tides and energy fluxes over great meteor seamount. *Ocean Science*, *3*(3), 441–449. https://doi.org/10.5194/os-3-441-2007

Gregg, M. C. (1989). Scaling turbulent dissipation in the thermocline. *Journal of Geophysical Research*, *94*(C7), 9686–9698. https://doi.org/10.1029/JC094iC07p09686

Gregg, M. C., & Kunze, E. (1991). Shear and strain in Santa Monica Basin. *Journal of Geophysical Research*, *96*(C9), 16,709–16,719. https://doi.org/10.1029/91JC01385

Gregg, M. C., Sanford, T. B., & Winkel, D. P. (2003). Reduced mixing from the breaking of internal waves in equatorial waters. *Nature*, *422*(6931), 513–515.

Haji, M. N. (2015). Thesis: Scattering of the low-mode internal tide at the Line Islands Ridge. https://hdl.handle.net/1912/7208 iModes download: http://web.mit.edu/endlab/downloads and https://sourceforge.net/projects/imodes/

Jayne, S. R., & St Laurent, L. C. (2001). Parameterizing tidal dissipation over rough topography. *Geophysical Research Letters*, *28*(5), 811–814. https://doi.org/10.1029/2000GL012044

Jungclaus, J. H., Keenlyside, N., Botzet, M., Haak, H., Luo, J.-J., Latif, M., et al. (2006). Ocean oirculation and tropical variability in the Coupled Model ECHAM5/MPI-OM. *Journal of Climate*, *19*, 3952.

Klymak, J. M., Pinkel, R., & Rainville, L. (2008). Direct breaking of the internal tide near topography: Kaena Ridge, Hawaii. *Journal of Physical Oceanography*, *38*(2), 380–399.

Köhler, J., Mertens, C., Walter, M., Stöber, U., Rhein, M., & Kanzow, T. (2013). Variability in the internal wave field induced by the Atlantic deep western boundary current at 16 °N. *Journal of Physical Oceanography*, *44*(2), 492–516.

Kunze, E. (2017). Internal-wave-driven mixing: Global geography and budgets. *Journal of Physical Oceanography*, *47*(6), 1325–1345.

Kunze, E., Firing, E., Hummon, J. M., Chereskin, T. K., & Thurnherr, A. M. (2006). Global abyssal mixing inferred from lowered ADCP shear and CTD strain profiles. *Journal of Physical Oceanography*, *36*(8), 1553–1576.

Lee, C. M., Sanford, T. B., Kunze, E., Nash, J. D., Merrifield, M. A., & Holloway, P. E. (2006). Internal tides and turbulence along the 3000-m isobath of the Hawaiian Ridge. *Journal of Physical Oceanography*, *36*(6), 1165–1183.

Li, Z., Storch, J.-S. v., & Müller, M. (2015). The M_2 internal tide simulated by a 1/10° OGCM. *Journal of Physical Oceanography*, *45*(12), 3119–3135. https://doi.org/10.1175/JPO-D-14-0228.1

Li, Z., von Storch, J.-S., & Müller, M. (2017). The K_1 internal tide simulated by a 1/10° OGCM. *Ocean Modelling*, *113*, 145–156.

MacKinnon, J. A., Alford, M. H., Pinkel, R., Klymak, J., & Zhao, Z. (2012). The latitudinal dependence of shear and mixing in the pacific transiting the critical latitude for PSI. *Journal of Physical Oceanography*, *43*(1), 3–16.

Marsland, S. J., Haak, H., Jungclaus, J. H., Latif, M., & Röske, F. (2003). The Max-Planck-Institute global ocean/sea ice model with orthogonal curvilinear coordinates. *Ocean Modelling*, *5*(2), 91–127.

Müller, M. (2013). On the space- and time-dependence of barotropic-to-baroclinic tidal energy conversion. *Ocean Modelling*, *72*, 242–252. https://doi.org/10.1016/j.ocemod.2013.09.007

Müller, M., Cherniawsky, J. Y., Foreman, M. G. G., & von Storch, J.-S. (2012). Global M_2 internal tide and its seasonal variability from high resolution ocean circulation and tide modeling. *Geophysical Research Letters*, *39*, L19607. https://doi.org/10.1029/2012GL053320

Müller, M., Cherniawsky, J. Y., Foreman, M. G. G., & von Storch, J.-S. (2014). Seasonal variation of the M_2 tide. *Ocean Dynamics*, *64*(2), 159–177. https://doi.org/10.1007/s10236-013-0679-0

Munk, W. (1981). Internal waves and small scale processes. In B. A. Warren & C. Wunsch (Eds.), *Evolution of physical oceanography* (pp. 264–290): The MIT Press.

Nash, J. D., Alford, M. H., & Kunze, E. (2005). Estimating internal wave energy fluxes in the ocean. *Journal of Atmospheric and Oceanic Technology*, *22*(10), 1551–1570. https://doi.org/10.1175/JTECH1784.1

Nash, J. D., Kunze, E., Lee, C. M., & Sanford, T. B. (2006). Structure of the baroclinic tide generated at Kaena Ridge, Hawaii. *Journal of Physical Oceanography*, *36*(6), 1123–1135.

Nycander, J. (2005). Generation of internal waves in the deep ocean by tides. *Journal of Geophysical Research*, *110*, C10028. https://doi.org/10.1029/2004JC002487

Olbers, D., & Eden, C. (2013). A global model for the diapycnal diffusivity induced by internal gravity waves. *Journal of Physical Oceanography*, *43*(8), 1759–1779.

Osborn, T. R. (1980). Estimates of the local rate of vertical diffusion from dissipation measurements. *Journal of Physical Oceanography*, *10*(1), 83–89.

Pacanowski, R. C., & Philander, S. G. H. (1981). Parameterization of vertical mixing in numerical models of tropical oceans. *Journal of Physical Oceanography*, *11*, 1443–1451.

Pollmann, F., Eden, C., & Olbers, D. (2017). Evaluating the global internal wave model IDEMIX using finestructure methods. *Journal of Physical Oceanography*, *47*(9), 2267–2289.

Polzin, K., Kunze, E., Hummon, J., & Firing, E. (2002). The finescale response of lowered ADCP velocity profiles. *Journal of Atmospheric and Oceanic Technology*, *19*(2), 205–224.

Rainville, L., Johnston, T. M. S., Carter, G. S., Merrifield, M. A., Pinkel, R., Worcester, P. F., & Dushaw, B. D. (2010). Interference pattern and propagation of the M_2 internal tide south of the Hawaiian Ridge. *Journal of Physical Oceanography*, *40*(2), 311–325.

Redi, M. H. (1982). Oceanic isopycnal mixing by coordinate rotation. *Journal of Physical Oceanography*, *12*, 1154–1154.

Richet, O., Muller, C., & Chomaz, J.-M. (2017). Impact of a mean current on the internal tide energy dissipation at the critical latitude. *Journal of Physical Oceanography*, *47*(6), 1457–1472.

Rimac, A., von Storch, J.-S., Eden, C., & Haak, H. (2013). The influence of high-resolution wind stress field on the power input to near-inertial motions in the ocean. *Geophysical Research Letters*, *40*, 4882–4886. https://doi.org/10.1002/grl.50929

Simmons, H. L., Hallberg, R. W., & Arbic, B. K. (2004). Internal wave generation in a global baroclinic tide model. *Deep Sea Research Part II: Topical Studies in Oceanography*, *51*(25–26), 3043–3068.

St. Laurent, L. C., & Garrett, C. (2002). The role of internal tides in mixing the deep ocean. *Journal of Physical Oceanography*, *32*(10), 2882–2899.

Steele, M., Morley, R., & Ermold, W. (2001). PHC: A global ocean hydrography with a high-quality Arctic Ocean. *Journal of Climate*, *14*(9), 2079–2087.

Storch, J.-S. v., Eden, C., Fast, I., Haak, H., Hernández-Deckers, D., Maier-Reimer, E., et al. (2012). An estimate of the Lorenz energy cycle for the world ocean based on the STORM/NCEP simulation. *Journal of Physical Oceanography*, *42*(12), 2185–2205.

Thomas, M., Sündermann, J., & Maier-Reimer, E. (2001). Consideration of ocean tides in an OGCM and impacts on subseasonal to decadal polar motion excitation. *Geophysical Research Letters*, *28*(12), 2457–2460. https://doi.org/10.1029/2000GL012234

Vic, C., Garabato, A. C. N., Green, J. A. M., Spingys, C., Forryan, A., Zhao, Z., & Sharples, J. (2018). The lifecycle of semidiurnal internal tides over the northern Mid-Atlantic Ridge. *Journal of Physical Oceanography*, *48*(1), 61–80.

Vic, C., Naveira Garabato, A. C., Green, J. A. M., Waterhouse, A. F., Zhao, Z., Melet, A., et al. (2019). Deep-ocean mixing driven by small-scale internal tides. *Nature Communications*, *10*(1), 2099. https://doi.org/10.1038/s41467-019-10149-5

von Storch, J.-S., Haak, H., Hertwig, E., & Fast, I. (2016). Vertical heat and salt fluxes due to resolved and parameterized meso-scale eddies. *Ocean Modelling*, *108*, 1–19.

Waterhouse, A. F., Kelly, S. M., Zhao, Z., MacKinnon, J. A., Nash, J. D., Simmons, H., et al. (2018). Observations of the Tasman Sea internal tide beam. *Journal of Physical Oceanography*, *48*(6), 1283–1297.

Whalen, C. B., MacKinnon, J. A., & Talley, L. D. (2018). Large-scale impacts of the mesoscale environment on mixing from wind-driven internal waves. *Nature Geoscience*, *11*(11), 842–847.

Whalen, C. B., MacKinnon, J. A., Talley, L. D., & Waterhouse, A. F. (2015). Estimating the mean diapycnal mixing using a finescale strain parameterization. *Journal of Physical Oceanography*, *45*, 1174–1188.

Zenk, W. (1970). On the temperature and salinity structure of the Mediterranean water in the northeast Atlantic. *Deep Sea Research and Oceanographic Abstracts*, *17*(3), 627–631.

Zhao, Z. (2018). The global mode-2 M_2 internal tide. *Journal of Geophysical Research: Oceans*, *123*, 7725–7746. https://doi.org/10.1029/2018JC014475

Zhao, Z., & Alford, M. H. (2009). New altimetric estimates of mode-1 M_2 internal tides in the Central North Pacific Ocean. *Journal of Physical Oceanography*, *39*(7), 1669–1684.

Zhao, Z., Alford, M. H., Girton, J., Johnston, T. M. S., & Carter, G. (2011). Internal tides around the Hawaiian Ridge estimated from multisatellite altimetry. *Journal of Geophysical Research*, *116*, C12039. https://doi.org/10.1029/2011JC007045

Zhao, Z., Alford, M. H., Girton, J. B., Rainville, L., & Simmons, H. L. (2016). Global observations of open-ocean mode-1 M_2 internal tides. *Journal of Physical Oceanography*, *46*, 1657–1684.